

Nanoscale

Accepted Manuscript

This article can be cited before page numbers have been issued, to do this please use: Z. Huang, Z. Yang, Q. Jia, N. Wang, Y. Zhu and Y. Xia, *Nanoscale*, 2022, DOI: 10.1039/D1NR07913A.



This is an Accepted Manuscript, which has been through the Royal Society of Chemistry peer review process and has been accepted for publication.

Accepted Manuscripts are published online shortly after acceptance, before technical editing, formatting and proof reading. Using this free service, authors can make their results available to the community, in citable form, before we publish the edited article. We will replace this Accepted Manuscript with the edited and formatted Advance Article as soon as it is available.

You can find more information about Accepted Manuscripts in the [Information for Authors](#).

Please note that technical editing may introduce minor changes to the text and/or graphics, which may alter content. The journal's standard [Terms & Conditions](#) and the [Ethical guidelines](#) still apply. In no event shall the Royal Society of Chemistry be held responsible for any errors or omissions in this Accepted Manuscript or any consequences arising from the use of any information it contains.

Bimetallic Co-Mo sulfide/carbon composites derived from polyoxometalate encapsulated polydopamine-decorated ZIF nanocubes for efficient hydrogen and oxygen evolution

Zheng Huang,^a Zhuxian Yang,^a Quanli Jia,^b Nannan Wang,^c Yanqiu Zhu^a and Yongde Xia^{*a}

^a *College of Engineering, Mathematics and Physical Sciences, University of Exeter, Exeter EX4 4QF, United Kingdom. Email: y.xia@exeter.ac.uk*

^b *Henan Key Laboratory of High Temperature Functional Ceramics, Zhengzhou University, Zhengzhou, 450052, PR China*

^c *GIFT (Guangxi Institute for Fullerene Technology), Key Laboratory of New Processing Technology for Nonferrous Metals and Materials, Ministry of Education, School of Resources, Environment and Materials, Guangxi University, Guangxi, 530004, China*

Abstract

View Article Online
DOI: 10.1039/D1NR07913A

The increased call on carbon neutrality by 2050 makes it compelling to develop emission-free alternative energy sources. Green hydrogen produced from water electrolyzer by renewable electricity is of great importance, and the development of efficient transition-metal-based materials for electrolysis hydrogen production is highly desirable. In this report, a new approach to produce electrocatalysts that are highly active for hydrogen and oxygen evolution reactions (HER and OER), defect-rich ultra-fine bimetallic Co-Mo sulfides on carbon composites from polyoxometalates@ZIF-67@polydopamine nanocubes via carbonization/sulfurization have been successfully developed. The coating of polydopamine (PDA) on the surface of the acid-sensitive ZIF-67 cubes can prevent the over-dissociation of ZIF-67 caused by encapsulated phosphomolybdic acid (PMA) etching through PDA chelating with the PMA molecules. Meanwhile, the partially dissociated Co^{2+} from the ZIF-67 can be captured by the coated PDA via chelation, resulting in more evenly dispersed active sites throughout the heterogeneous composite after pyrolysis. The optimized bimetallic composite CoMoS-600 exhibits a prominent improvement in HER (with overpotential of -0.235 V vs. RHE at current density of 10 mA cm^{-2}) and OER performance (with overpotential of 0.350 V vs. RHE at current density of 10 mA cm^{-2}), due to the synergistic effect of ultra-fine defect-rich Co-Mo-S nanoparticle active sites and N, S-doped porous carbons in the composites. Moreover, this synthesis approach can be readily expanded to other acidic polyoxometalates to produce HER and OER active bimetallic Co-W sulfide/carbon composites by replacing PMA with phosphotungstic acid. This new synthesis strategy to modify acid-sensitive ZIFs with selected compounds offers an alternative approach to develop novel transition metal sulfide/carbon composites for various applications.

Keywords: *ZIF; Metal sulfide; Composite; Hydrogen evolution reaction; Oxygen evolution reaction*

1. Introduction

Due to its high-energy density and zero-emission, hydrogen is the most promising sustainable energy carrier in the future. Under the increased call on carbon neutrality by 2050, green hydrogen produced from water splitting via electrolyzer driven by renewable electricity or solar light-based photocatalysis is of great interest.¹⁻⁴ The efficiency of the electrolyzer is one of the bottlenecks toward cheap and large-scale hydrogen production, which can be improved by efficient electrocatalytic materials. The current benchmark electrocatalysts for the cathodic hydrogen evolution reaction (HER) and anodic oxygen evolution reaction (OER) are Pt and IrO₂/RuO₂ respectively,⁵ but both are noble metals, which is undesirable for commercial applications. Therefore, developing cost-effective transition-metal-based electrocatalysts are highly desirable.

Two-dimensional layered transition metal dichalcogenides (2D TMDs) have been one of the most popular material families for electrochemical energy-related applications due to their unique structures and intrinsic properties.^{6,7} MoS₂ is one of the most well-studied materials in the 2D TMDs family. Both theoretical simulations and experimental works confirm that the unsaturated chalcogens and metals on the exposed edges are the active sites for the HER reactions.^{8,9} However it is well known that MoS₂ possesses poor OER activities.¹⁰ To develop bifunctional catalysts that are active towards both HER and OER, hybridising MoS₂ with 3d transition metal (i.e. Co, Fe or Ni) sulfides have been extensively adopted.¹¹ This multi-interface engineering strategy can also improve the conductivity and adsorption of electrochemical intermediates of the electrocatalyst.¹² In particular, cobalt sulfides incorporated MoS₂ have been widely explored. For example, recently Huang et al. have synthesised a mesoporous CoS/MoS₂ for water splitting application,¹³ Ganesan et al. have created a multi-shelled CoS₂-MoS₂ hollow sphere for efficient water splitting,¹⁴ and Gao et al. have assembled a core-shell Co₃S₄@MoS₂ for both HER and OER.¹⁵

Besides introducing cobalt into MoS₂, the electrochemical efficiency of the electrocatalysts can be strategically promoted by active site engineering strategies, including edge-site formation, nano-sized TMD and highly curved structures formed on the MoS₂ crystals.¹⁶ Those ultra-fine open-ended nanostructures and rich defects enable the catalysts to expose a higher density of active sites for the key reactions, consequently leads to improved electrocatalytic activity.^{17, 18} In order to maintain the fine nanostructure of electrocatalysts, to prevent heat-induced sintering¹⁹ and high surface energy induced agglomeration of the active components,²⁰ graphitic carbon matrix can be introduced to isolate the electrocatalytic active MoS₂ nanoparticles.^{21, 22} Meanwhile, the excellent electronic conductivity of graphitic carbon benefits fast charge transfer in the composites, resulting in enhanced activities.^{22, 23} More interestingly, porosity can be introduced into the graphitic carbon matrix. As a result, the porous graphitic carbon matrix can not only isolate the electrocatalytic active sites to avoid agglomeration, but also promote the mass transports during the electrocatalytic reactions, thereby enabling the active sites to be readily accessible by reactants.²⁴ Moreover, the porous carbon matrix can be doped with heteroatoms such as N and/or S, which can modulate the electronic structure of the composites and create more catalytic active sites, therefore further improving the electrocatalytic activities of the heterostructured composites.²⁵ Built on the above considerations, the porous zeolitic imidazolate framework (i.e. ZIF-67) is an ideal precursor to develop heteroatom functionalized carbon-rich and transition metal Co-based composites.

Previously, we reported HER and OER active WS₂/Co_{1-x}S/porous carbon nanocomposites derived from in-situ synthesized polyoxometalates (POM)@ZIF-67.²⁶ However, since ZIF-67 is unstable in acidic environment,²⁷ attempts to in-situ synthesize Mo-containing counterpart via a similar method were unsuccessful due to the strong acidity and the uncertainty of molecular weight of phosphomolybdic acid hydrate (PMA, a Mo-containing

POM).²⁸ In this work, we developed an acid-resistance polydopamine (PDA) coating²⁹ on the pre-synthesized ZIF-67 as a buffer layer to protect ZIF-67 from PMA etching, and to synthesize PMA modified ZIF-67 composite PMA@ZIF-67@PDA. Moreover, Tris-buffer solution for dopamine polymerization is further used to avoid drastic dissociation of the ZIF when the strong acidic PMA is introduced. In this synthesis strategy, N-containing PDA can also act as another N source for N-doping besides the organic linker 2-Methylimidazole (MeIM) in ZIF-67. Since the PDA decorated on hydrophobic surfaces is less stable to acid medium than on hydrophilic surfaces,²⁹ cetyltrimethylammonium bromide (CTAB) was added during the synthesis of ZIF-67 in order to tune the hydrophobic surface of ZIF³⁰ into a hydrophilic surface. Meanwhile, the addition of CTAB has led to the cubical morphology of ZIF-67 crystals. In addition, PDA not only protects ZIF-67 from the strong acidity of PMA, but also provides rich functional groups that have strong chelating capability with metal ions. Therefore PDA can chelate with free PMA molecules as well as Co²⁺ dissociated from the ZIF, which results in an increased amount of active sites in the final derivatives. One-step carbonization and sulfurization of the as-synthesized PMA@ZIF-67@PDA at high temperature in hydrogen sulfide atmosphere can generate bimetallic Co-Mo sulfide supported on carbon nanocomposites. The optimized Co-Mo-S@N, S-doped porous carbon composites exhibit significantly enhanced HER and OER performance compared with the counterparts derived from ZIF-67 nanocubes. This synthesis approach can be further expanded to synthesize phosphotungstic acid (PTA)@ZIF-67@PDA, and the corresponding derivatives are also good electrocatalysts with enhanced performance in HER and OER.

2. Experimental

All reagents, including Cobalt (II) nitrate hexahydrate (Co(NO₃)₂·6H₂O, 99%), 2-Methylimidazole (C₄H₆N₂, 99%, abbreviated as MeIM), Phosphomolybdic acid hydrate (H₃PMo₁₂O₄₀·xH₂O, abbreviated as PMA), Phosphotungstic acid hydrate (H₃PW₁₂O₄₀·xH₂O,

abbreviated as PTA), Cetyltrimethylammonium bromide ($C_{19}H_{42}BrN$, 99+%, abbreviated as CTAB), TRIS-buffer solution (0.5 M, pH=8.5) and Dopamine hydrochloride ($C_8H_{11}NO_2 \cdot HCl$, 99%), were purchased from Fisher Scientific and used without further purification.

2.1 Synthesis of ZIF-67 nanocubes

ZIF-67 nanocubes (Z67) were synthesized based on the previous report with slight modification to scale up the production.³¹ In a typical synthesis, 1.16 g of $Co(NO_3)_2 \cdot 6H_2O$ and 0.02 g of CTAB were dissolved in 40 ml of distilled water while 18.16 g of MeIM was dissolved in 280 ml of distilled water separately. The mixture of $Co(NO_3)_2 \cdot 6H_2O$ and CTAB was then rapidly poured into the MeIM solution under vigorous stirring at 500 RPM, followed by continuously stirring for 20 min at room temperature. The purple powder was collected by centrifugation at 7000 RPM for 5 min and washed twice by water and once by ethanol. The obtained sample was dried in a fume hood for 2 days and stored in a glass vial for further treatment.

2.2 Synthesis of POM@ZIF-67@PDA nanocubes

To obtain PMA@ZIF-67@PDA nanocubes (Mo-Z67-D), three solutions were prepared in advance: solution A, 34 ml of 0.01 M Tris-buffer solution was prepared by adding 2 ml 0.5 M Tris-buffer solution (pH=8.5) into 32 ml of distilled water; solution B, 0.05 g of dopamine hydrochloride was dissolved in 17 mL of distilled water; solution C, 0.2 g PMA was dissolved in 50 ml distilled water. Then 0.15 g of dried ZIF-67 powder was dispersed in 51 mL of distilled water under sonication for 5 min. An extra 1 mL of ethanol was added before the water to achieve better dispersion of the hydrophobic ZIF nanocubes. The ZIF-67 dispersion solution was stirred at 500 RPM, followed by the addition of solutions A and B. The polydopamine started to decorate and coat on the surface of the ZIF-67 nanocubes, changing the colour of the mixture from purple to dark purple. Then solution C was introduced, and the mixture was kept stirring for another 20 min. Finally, the resultant composite was collected via centrifugation at

7000 RPM and washed with ethanol three times. The obtained sample was dried in a fume hood for 2 days. PTA@ZIF-67@PDA nanocubes (W-Z67-D) were synthesized via a similar procedure for the synthesis of Mo-Z67-D, except the replacement of PMA solution by the same amount of PTA solution. In addition, ZIF-67@PDA nanocubes (Z67-D) were also prepared for comparison, following the same procedure for the synthesis of Mo/W-Z67-D, only replacing the PMA/PTA solution with the same amount of distilled water.

2.3 Synthesis of bimetallic Co-Mo and Co-W sulfide/carbon composites

The as-synthesized Z67 as well as the Mo-Z67-D and W-Z67-D were then subjected to pyrolysis at three different temperatures (600, 800 and 1000 °C) to obtain a series of carbon-based nanocomposites. In a typical synthesis, 0.05 g of dry sample powder was loaded into a ceramic boat and pyrolyzed in a flow-through tube furnace in Ar with a flow rate of 50 mL min⁻¹ and heating ramp rate of 10 °C min⁻¹ or 2 °C min⁻¹. After reaching the target pyrolysis temperature, H₂S gas was introduced into the tube for 1 hour. Followed by the sulfurization/carbonization process, the sample was naturally cooled down to room temperature under Ar flow. The obtained samples were named CoMoS-X or CoWS-X, where X stands for the pyrolysis temperature of the samples. For samples obtained under a heating rate of 10 °C min⁻¹ an extra “-10” was added in the sample names. For example, CoMoS-600 refers to sample derived from Mo-Z67-D at pyrolysis temperature of 600 °C and heating ramp rate of 2 °C min⁻¹, whereas CoWS-800-10 refers to sample derived from W-Z67-D at pyrolysis temperature of 800 °C and heating ramp rate of 10 °C min⁻¹. PMA and PTA were also heated at 800 °C under the same H₂S/Ar atmosphere for comparison, and the obtained samples were designated as PMA-C and PTA-C respectively.

2.4 Materials characterization

Powdered X-ray diffraction (XRD) was taken under Cu-K α radiation at 40 mA and 40 kV using a Bruker D8 advanced X-ray diffractometer. Fourier-transform infrared (FT-IR) spectra were

recorded on a Shimadzu IRTracer-100 spectrometer at wavelength of 500-1300 cm^{-1} . Samples were prepared by KBr pellet method. Thermogravimetric analysis (TGA) was performed on a TA SDT Q600 instrument with target temperature of 800 $^{\circ}\text{C}$ and heating ramp rate of 10 $^{\circ}\text{C}$ min^{-1} in air with flow rate of 100 mL min^{-1} . N_2 gas sorption analysis was carried out on a Quantachrome AutosorbIQ gas sorptometer with outgas temperature at 150 $^{\circ}\text{C}$ for 3 hours. Brunauer-Emmett-Teller (BET) method was used to calculate the surface area of the samples, based on the adsorption data in the partial pressure (P/P_0) range of 0.05-0.2. Total pore volume was determined from the amount of adsorbed N_2 at P/P_0 ca. 0.99. Raman spectra were acquired on a Renishaw inVia Raman microscope with excitation laser beam of 532 nm using a 20 \times objective lens. Helios Nanolab 600i scanning electron microscope/Focused ion beam DualBeam workstation was used to acquire scanning electron microscopy (SEM) images. Samples were splattered with gold to reduce the effect of charging. Transmission electron microscopy (TEM) images were obtained on a JOEL-2100 LaB6 transmission electron microscope. Samples were first dispersed by sonication in absolute ethanol for 10 min and then deposited on a holey carbon copper grid. X-ray photoelectron spectroscopy (XPS) was carried out on a Kratos Axis Ultra system with monochromated Al Kr X-ray source operated at 10 mA emission current and 15 kV anode potential.

2.5 Electrocatalytic measurements

Electrochemistry measurements of the samples were carried out on a CHI660E electrochemical workstation with a three electrodes setup: 3 mm glassy carbon as working electrode, Ag/AgCl as reference electrode and carbon rod as the counter electrode. HER was evaluated in 0.5 M H_2SO_4 solution, while OER was tested in O_2 -saturated 1 M KOH solution. The O_2 -saturated electrolyte was prepared by purging O_2 for 20 min before the test, and the working electrode was spun at 1600 rpm during the OER measurement. Sample ink was prepared by dispersing 3 mg of the sample in 1 mL of water/ethanol (4:1 v/v) solution and 5 μL of 5 wt% Nafion

solution for 30 min in the ultrasonic bath. 5 μL of the ink was drop cast onto the 3 mm mirror-finished glassy carbon electrode and left dry before the test.

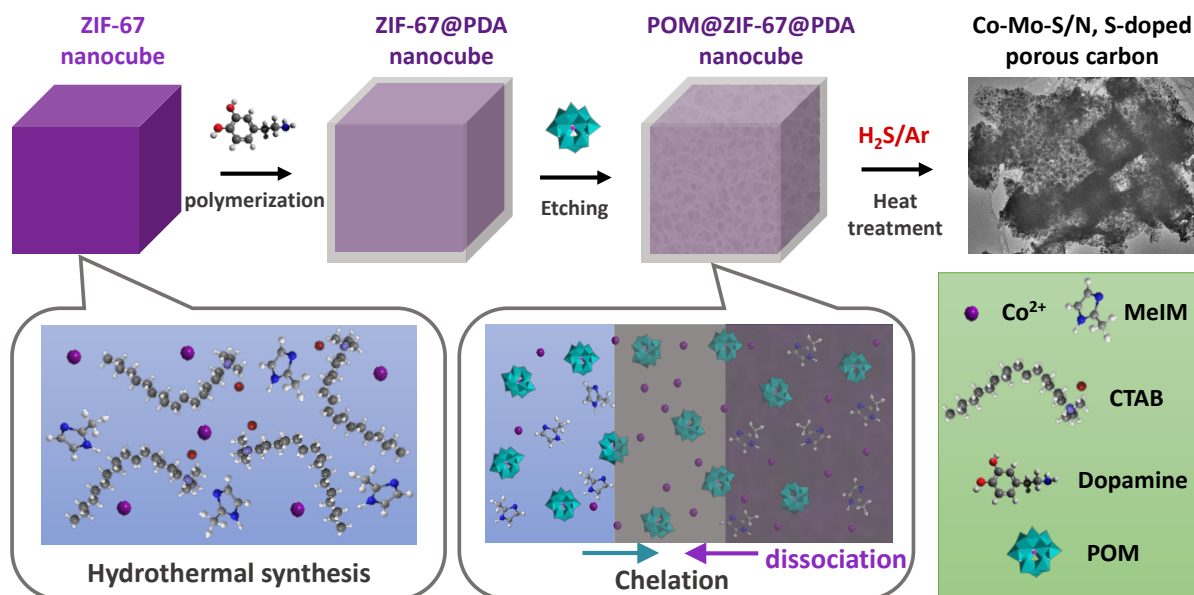
To activate the catalysts and obtain stable results, 30 cyclic voltammetry (CV) cycles were scanned before conduct linear sweep voltammetry (LSV) measurements. iR-correction was applied with a compensation level of 95% to eliminate the effect of uncompensated solution resistance. All the potentials are converted to and reported vs. the potentials of the reversible hydrogen electrode (RHE). The conversion is achieved via the Nernst equation ($E_{RHE} = E_{Ag/AgCl} + 0.059 \times (\text{pH}) + 0.197$, where pH is the pH value of the electrolyte solution). The reaction kinetic is interpreted by the Tafel slope, which is calculated from the Tafel equation ($\eta = a + b \log(j)$, where η is the overpotential, j is the exchange current density and a is the interception). By plotting the potential versus the current density in logarithm and fitting the linear portion of the plot, Tafel slope can be easily obtained. Electrochemical impedance spectroscopy (EIS) was conducted in the frequency range of 100 kHz - 0.1 Hz, at the overpotential to achieve a current density of 10 mA cm⁻² (η_{10}) of the catalysts.

3. Results and discussion

3.1 Characterization of the as-synthesized PMA@ZIF-67@PDA nanocubes

As shown in Scheme 1, to obtain the precursor POM@ZIF-67@PDA nanocubes, cubical ZIF-67 was first synthesized at room temperature via the hydrothermal method in the presence of surfactant CTAB. ZIF-67@PDA nanocubes were then synthesized by depositing a thin layer of PDA on the surface of the ZIF-67 nanocubes via in-situ polymerization. Finally, POM (i.e. PMA or PTA) was introduced into the ZIF-67@PDA solution. The acidic POM molecules can penetrate through the PDA coating layer outside the ZIF-67 cubes and reach the ZIF-67 cubes, resulting in partly dissociation of the ZIF-67 core. Meanwhile, the Co²⁺ dissociated from the ZIF-67 by acid etching, as well as some of the POM molecules were stuck in the PDA layer

via functional group chelation. The obtained POM@ZIF-67@PDA nanocubes were then subjected to one-step carbonization/sulfurization at high temperatures in H₂S/Ar atmosphere to derive bimetallic Co-Mo-S/N, S-doped porous carbon composites as HER and OER catalysts.



Scheme 1 Diagram of the synthesis of POM@ZIF-67@PDA precursor and bimetallic Co-Mo-S/N, S-doped porous carbon composites.

The SEM images (Fig. 1) of all the as-synthesized precursors present highly uniform cubic nanoparticles with diameter of around 600 nm. The pristine ZIF-67 nanocubes (Z67) have a smooth surface compared to the other three PDA decorated samples. With the PDA coating and the POM (i.e. PMA or PTA) modification, the surfaces of the cubes have become rough and lumpy. TEM image (insert in Fig. 1A) and elemental mapping (Fig. S1A) show that homogeneous ZIF-67 cubes are formed with the help of surfactant CTAB. After the deposition of PDA, Z67-D is obtained with a thin layer of PDA coated on the surface of the cubes (insert in Fig. 1B). Oxygen rich outer layer is found in the corresponding elemental mapping (Fig. S1B), which also confirms the formation of PDA coating. With the incorporation of PMA, Mo-Z67-D shows a well-defined cubical shape with a porous interior (insert in Fig. 1C). It is believed that the acidic PMA molecules can penetrate through the acid-resistant PDA coating²⁹

and react with the acid intolerance ZIF core, leading to partial dissociation of the ZIF-67 structure, which is consistent with the previous report.³¹ Accumulation of Mo, O and P elements are observed on the nanocube surface from the elemental mapping in Fig. S1C, revealing that some PMA molecules have stuck in the coating layer via chelation with PDA functional groups. It is likely that the chelation mechanism of the PMA is as follows: At high pH (resulted from the tris-buff solution, pH=8.5), PMA may undergo a series of hydrolysis reactions, leading to the formation of lacunary phosphomolybdates.^{32,33} Some of the negatively charged lacunary phosphomolybdates and the shed charged Mo species such as MoO_4^{2-} and MoO_2^{2+} can then chelate with the functional groups of PDA.^{34,35} Moreover, a small amount of C and Co is found in the outer layer of cubes as well, indicating that trace amount of free Co^{2+} from the dissociation of ZIF-67 has chelated with coated PDA. Elemental line scanning of the samples (Fig. S2A, B and C) re-affirm the effect of PMA on the morphology of the composite and the chelation of PMA with the coated PDA.

All the modified samples show characteristic XRD peaks of ZIF-67 (Fig. S3A), indicating the basic ZIF-67 structure is retained in these modified samples irrespective of the PDA coating or the introduction of PMA. Both Z67-D and Mo-Z67-D show a slight decrease in the intensity of the characteristic diffraction peaks, possibly due to the partial dissociation of ZIF core caused by PDA coating and PMA etching. The FT-IR spectra (Fig. S3B) are in good agreement with the XRD results, revealing that the ZIF-67 structure is not significantly affected by the presence of CTAB, PDA coating and the PMA etching. Mo-Z67-D shows the characteristic peaks of both ZIF-67 and PMA, confirming the successful introduction of PMA. The slight peak shift and splitting of the PMA peaks of the modified structure are attributed to the change of chemical environment^{21,26} and the dissociation of PMA itself due to the high pH value (pH=8.5) during the synthesis process.³²

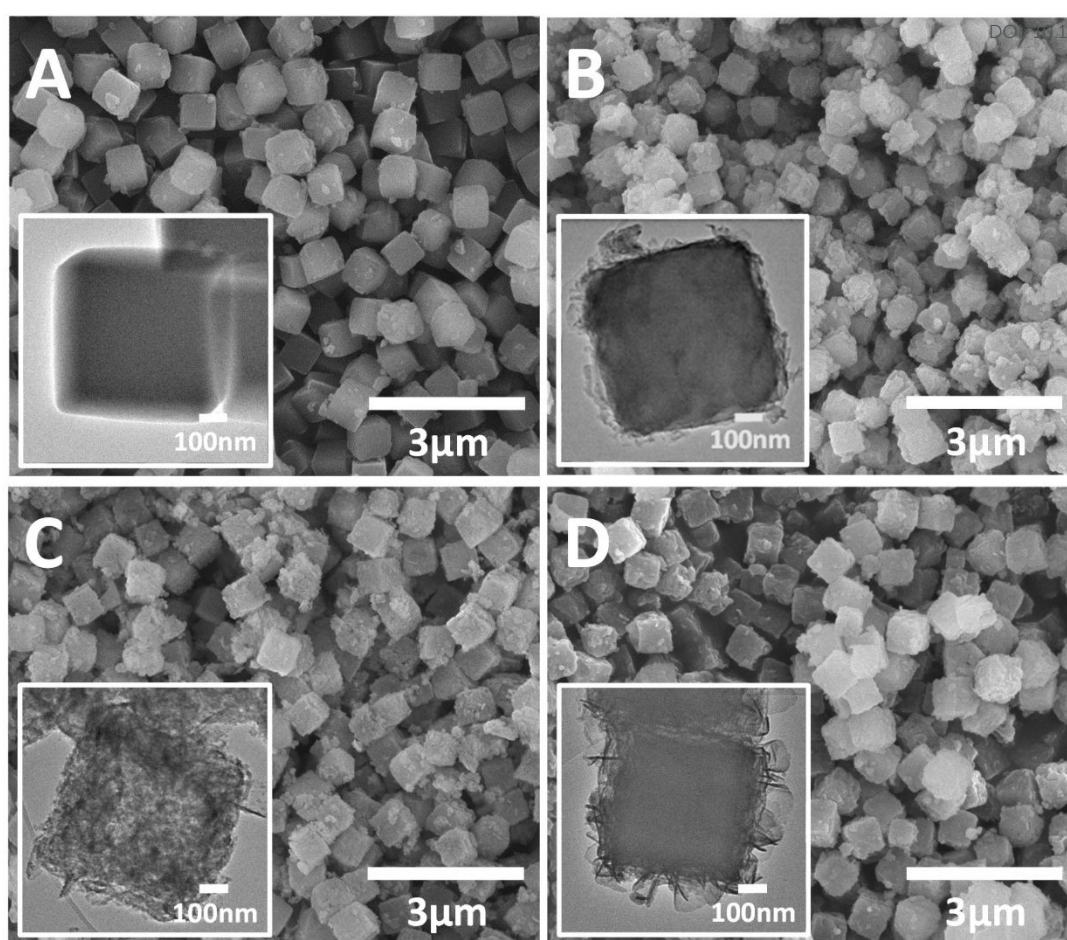


Fig. 1 SEM and TEM images (inserts) of A) Z67, B) Z67-D, C) Mo-Z67-D and D) W-Z67-D.

Textural properties of the as-synthesized samples were analyzed by nitrogen gas sorption, and the obtained isotherms and pore size distributions are shown in Fig. S3C. All samples exhibit typical type I isotherm based on the IUPAC classification, which is associated with the microporous structure of ZIF-67.³⁶ Small hysteresis loops are observed for Z67-D and Mo-Z67-D, possibly due to a small amount of micropores being destroyed by the etching and hydrolysis of ZIF-67, which results in pores larger than 2 nm.³⁷ The same conclusion can also be drawn from the pore size distributions of the modified samples (insert in Fig. S3C), in which larger pores with a diameter of 2-8 nm are observed. Moreover, macropores are found for the Mo-Z67-D sample at $P/P_0 \geq 0.8$,³⁸ suggesting the formation of hierarchical pores in this sample, which is in good agreement with TEM results. The BET surface area (S_{BET}) and total

pore volume (V_{total}) of the as-synthesized samples are summarized in Table S1. The surface area drops from $1549 \text{ m}^2 \text{ g}^{-1}$ for Z67 to 1123 and $1037 \text{ m}^2 \text{ g}^{-1}$ for Z67-D and Mo-Z67-D respectively. While Z67-D shows no significant change in V_{total} , Mo-Z67-D exhibits a prominent increase in V_{total} which further confirms that a large amount of pores are generated due to PMA etching. This observation is in good agreement with the above TEM results.

3.2 Characterization of PMA@ZIF-67 derived nanocomposites

Bimetallic Co-Mo-S/C nanocomposites can be readily produced via one-step sulfurization/carbonization of the as-synthesized Mo-Z67-D in $\text{H}_2\text{S}/\text{Ar}$ atmosphere at three different temperatures with variable ramp rates. XRD patterns in Fig. 2A show that these Mo-containing composites mainly present characteristic diffraction peaks attributed to $\text{CoMoS}_{3.13}$ (JCPDS #16-0439), accompanied by a trace amount of Mo_4O_{11} (JCPDS #13-0142) and Mo_2S_3 (JCPDS #40-0972). In contrast, Z67 derived sample CoS-1000 only shows the characteristic peaks of Co_{1-x}S (JCPDS #42-0826), which is in good agreement with our previous works.^{26, 39} This confirms that CTAB surfactant, PDA coating and the shape of the ZIF-67 crystal do not affect the composition of the pyrolyzed samples. The XRD patterns of Mo-Z67-D derived samples at various temperatures, and heating rates are presented in Fig. 2B. It is found that the crystallinity of the metal sulfides in the composites improved with elevated pyrolysis temperature and a slower ramp rate. Moreover, there are more oxidized species in sample that is pyrolyzed at $600 \text{ }^\circ\text{C}$ than those that is pyrolyzed at $1000 \text{ }^\circ\text{C}$. The shift of peak position and the broadening of the asymmetrical peak (see Fig. S4A) of samples obtained at lower pyrolysis temperature indicate that the metal sulfide in CoMoS-600 and CoMoS-600-10 possess smaller crystal sizes, possibly due to the non-uniform lattice distortions and crystallographic defects.⁴⁰ Obviously, the introduction of PMA prominently changes the composition of the composites. It is worth mentioning that no diffraction peaks from oxides are observable in the Z67 nanocube derived samples, but diffraction peaks for both MoO_2 and MoS_2 appear in sample PMA-C (Fig.

S4B), implying that the oxygen element is likely originated from the coated PDA and PMA molecules.

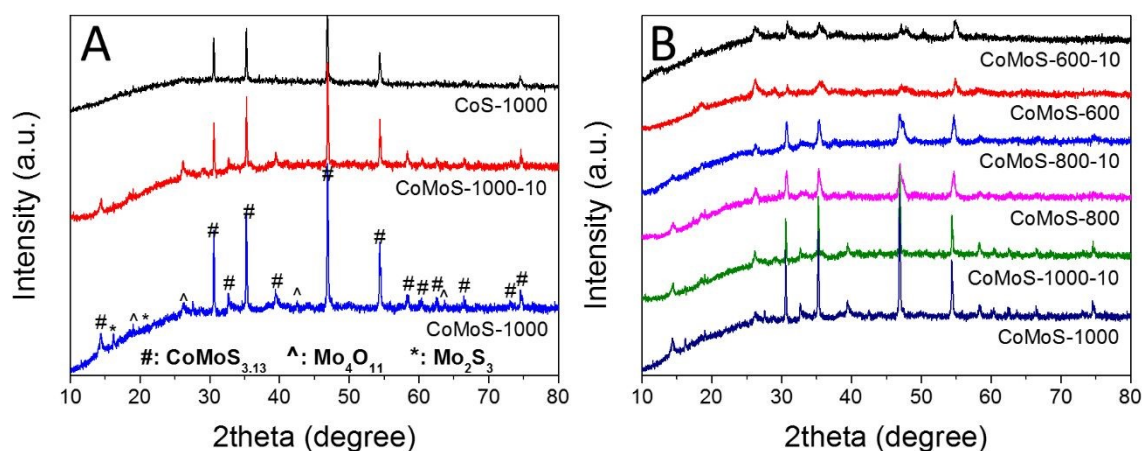


Fig. 2 XRD patterns of A) CoS-1000, CoMoS-1000-10 and CoMoS-1000 and B) samples derived from Mo-Z67-D at 600, 800, 1000 °C with heating ramp rate of 10 and 2 °C min⁻¹ respectively.

The Raman spectra of all the bimetallic Co-Mo-S/C samples (Fig. S5A and B) exhibit broad peaks with pronounced G band and D band. The G band at around 1593 cm⁻¹ is associated with the in-plane stretching of the graphite lattice, whereas the D band at around 1342 cm⁻¹ indicates the presence of a disordered band caused by the breathing mode of the graphite edges.⁴¹⁻⁴³ These results indicate that the amorphous sp²-hybridized carbon with a high density of defects dominates the carbon matrix originated from the carbonization of ZIF-67. Moreover, the degree of the graphitization of carbon in the composites can be estimated by the relative intensity between the two bands (i.e. I_D/I_G). As shown in Table S2, the I_D/I_G ratio decreases with the increase of pyrolysis temperature and slower heating ramp rate due to the formation of more graphitic carbon. It is well recognized that the degree of graphitization of carbon can affect the conductivity of the carbon matrix⁴⁴ and hence alter the charge transfer kinetics of the composites, which may contribute to the better electrocatalytic performance of the carbon-based catalysts.⁴⁵⁻⁴⁷

The morphology of the composites was first investigated by SEM. As shown in Fig. 3A, CoS-600 shows a nanocube morphology similar to the parental Z67. By increasing the pyrolysis temperature to 800 °C, nanocubes with the concave surface are observed for sample CoS-800 (Fig. 3B). Further increasing the pyrolysis temperature to 1000 °C, sample CoS-1000 shows distorted concave nanocube morphology decorated with small particles on the surface (Fig. 3C). In contrast, Mo-Z67-D derived CoMoS-600 shows mixed morphologies (Fig. 3D) of nanocubes, nanocube fragments with cracks and squared flakes. This observation further confirms that the PMA molecules not only chelate with the coated PDA, but also penetrate through the PDA coating to the inner core of the Mo-Z67-D leading to the etching of the inner core. The etching induced porous core is prone to collapse even at low pyrolysis temperature. More nanocube fragments decorated with small particles on the surface can be observed in sample CoMoS-800 (Fig. 3E). As pyrolysis temperature increased to 1000 °C, all nanocubes collapsed, and larger irregular particles appeared in sample CoMoS-1000 (Fig. 3F).

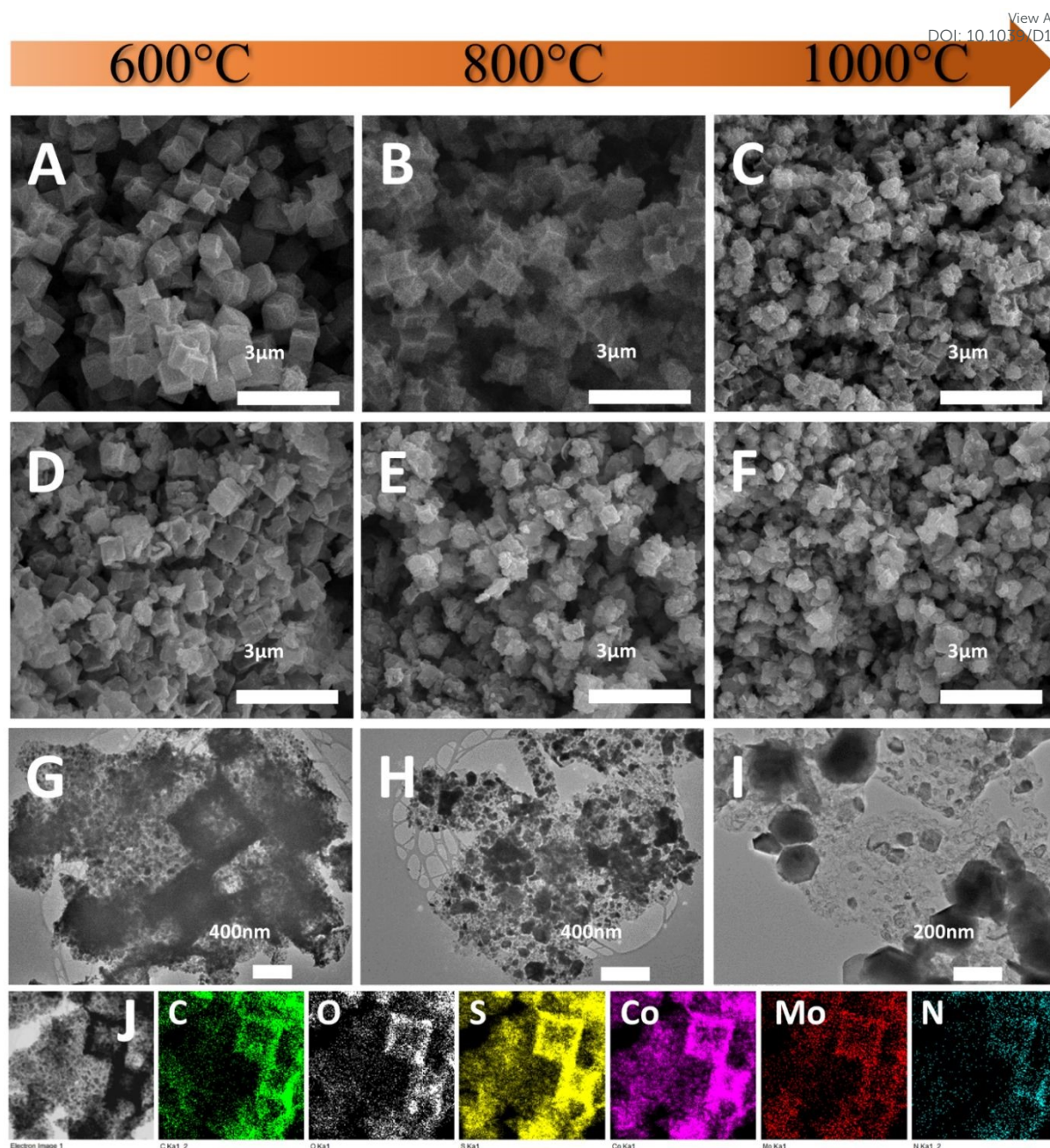


Fig. 3 SEM images of A) CoS-600, B) CoS-800, C) CoS-1000, D) CoMoS-600, E) CoMoS-800, F) CoMoS-1000; TEM images of G) CoMoS-600, H) CoMoS-800, I) CoMoS-1000 and J) Elemental mappings of CoMoS-600 obtained from TEM.

The morphologies of Mo-Z67-D derived composites were further investigated by TEM. As shown in Fig. 3G, a large number of fine nanoparticles are formed at 600 °C, which are evenly distributed in the carbon matrix. The elemental mappings of sample CoMoS-600 in Fig.

3J show that all elements including C, O, S, Co, Mo and N are evenly distributed throughout the carbon matrix, but no P element is detected in the sample, possibly due to the high volatility of elemental phosphorus at high temperature. When the pyrolysis temperature increases to 800 °C (Fig. 3H), the small particles agglomerate to form larger particles with sizes up to 200 nm. Smaller particles are still embedded in the carbon matrix, while larger ones accumulate at the edge of the matrix. For the sample obtained at 1000 °C (Fig. 3I), severe agglomeration is observed, and most of the metal sulfide particles migrate away from the carbon matrix to form aggregated large particles with sizes up to 500 nm. The elemental mappings of both CoMoS-800 and CoMoS-1000 are shown in Fig. S6. Similar to the sample obtained at 600 °C, elements C, O, S, Co, Mo and N are detected for both CoMoS-800 and CoMoS-1000 composites. The agglomerated metal sulfide particles are dominated by Co, Mo and S elements, which is in good agreement with the aforementioned XRD results. Small amount of thin flakes that mainly contain Mo and S are observed for the sample CoMoS-1000, which may be the formed Mo_2S_3 particles.⁴⁸ Based on the TEM-EDX results (see Table S3), Co/Mo ratio for CoMoS-600 is approximately 4.6:1, very close to 4.5:1 for the parental Mo-Z67-D.

The fine microstructures of the Mo-Z67-D derived bimetallic Co-Mo-S/C composites were studied via TEM and presented in Fig. 4. Comparing the samples obtained at different temperatures (Fig. 4 A, B and C), it is obvious that a large number of nanoparticles with maximum diameters of 20 nm are embedded in or supported on the amorphous carbon matrix for sample CoMoS-600. Higher pyrolysis temperature results in remarkably increased particle sizes. As shown in Fig. 4A, A1, A2 and A3, sample CoMoS-600 contains large amounts curved lattices and grain boundaries. The lattice spacings of three kinds of nanoparticles are found as labelled in the images, where the d-spacing of 0.56 nm corresponds to Mo_4O_{11} ;⁴⁹ 0.54 nm belongs to Mo_2S_3 ,⁵⁰ while 0.62 and 0.29 nm are related to $\text{CoMoS}_{3.13}$.⁵¹ The interlayer distances of $\text{CoMoS}_{3.13}$ vary in the range of 0.62 — 0.75 nm, which could be due to the formation of large

amounts of lattice distortion and defects in the 1-3 layers of $\text{CoMoS}_{3.13}$ crystals, which may benefit the electrochemical performance.^{52, 53} SAED pattern in the insert of Fig. 4A indicates the polycrystalline nature of sample CoMoS-600 and that the $\text{CoMoS}_{3.13}$ is the dominant crystalline phase of the composite. In samples CoMoS-800 and CoMoS-1000 (Fig. 4B and C), larger and thicker metal sulfide particles are clearly observed. The high-resolution TEM image in Fig. S7A for sample CoMoS-800 shows that a more intact $\text{CoMoS}_{3.13}$ crystal structure is formed with an increased number of layers and reduced interlayer distances (ranging from 0.62-0.66 nm). Compared to the composite obtained at 600°C, sample CoMoS-800 exhibits fewer defects in the crystals. For sample CoMoS-1000, most metal sulfides agglomerate to form large particles (Fig. S7B and C). Moreover, compared with samples CoMoS-600/800, sample CoMoS-1000 exhibits $\text{CoMoS}_{3.13}$ crystals with further increased thickness inside the carbon matrix (Fig. S7D). In addition, the interlayer distance of $\text{CoMoS}_{3.13}$ in sample CoMoS-1000 is exactly 0.62 nm, indicating the reduction of defects at high pyrolysis temperature. Graphitic carbon is observable in CoMoS-1000, as shown in Fig. S7E. These TEM observations are well in line with the above XRD results.

Texture properties of the three Co-Mo-S/C composites obtained at different pyrolysis temperatures are summarized in Table S4. Both BET surface area and total pore volume are in the order of CoMoS-800 > CoMoS-1000 > CoMoS-600, with CoMoS-800 possessing the highest surface area and pore volume, which can benefit mass and ion transportation during the electrochemical reactions.

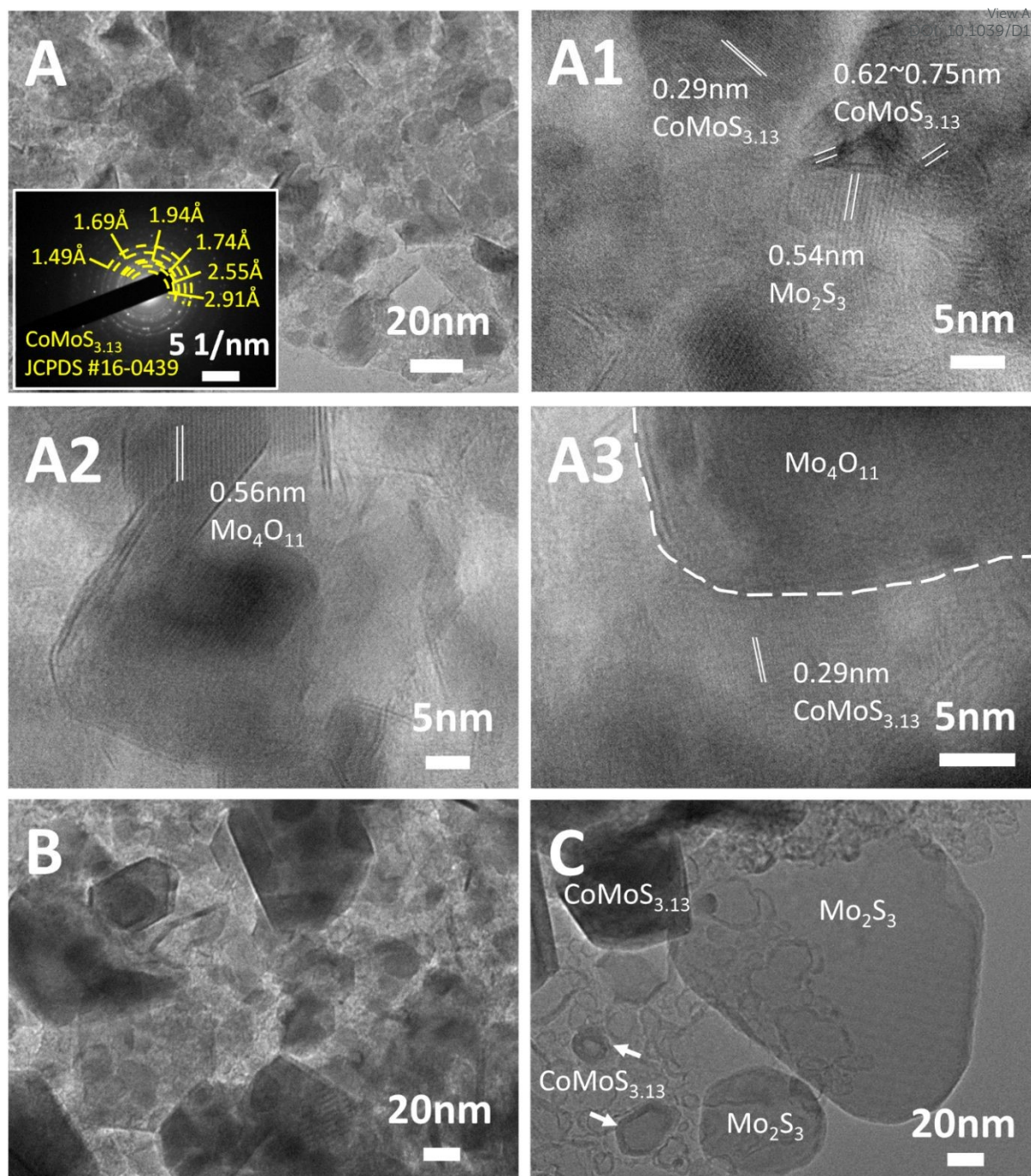


Fig. 4 TEM images of A) CoMoS-600, B) CoMoS-800 and C) CoMoS-1000. The insert in A) is the SAED pattern of CoMoS-600. A1), A2) and A3) are high resolution TEM images of CoMoS-600.

The surface chemistry of the samples was analyzed by XPS. The XPS element survey is presented in Fig. S8A, which confirms the presence of O, C, N, S and Co in the samples derived

from both the Mo-modified and PDA decorated ZIF67 and the pristine Z67, whereas the Mo element only appears in the Mo-modified samples. This is consistent with the XRD and elemental mapping results. In addition, only a trace amount of P is detected in sample CoMoS-600, which is negligible in composites CoMoS-800 and CoMoS-1000 (Fig. S8B) due to the high volatility of the elemental P during the pyrolysis. This small amount of P may lead to extra active sites in the Co-Mo-S/C composites, which contributes to the extraordinary electrochemistry performance of the composites.^{54, 55}

High-resolution XPS spectra of Mo 3d for samples CoMoS-600, CoMoS-800 and CoMoS-1000 are presented in Fig. 5A. The peak at ca. 227 eV is assigned to the S 2s peak due to the overlapping of Mo 3d and S 2s. Three doublets at around 229.4/232.5 eV, 231.8/234.9 eV and 233.4/236.5 eV are assigned to Mo 3d_{5/2} and 3d_{3/2} peaks of Mo⁴⁺, Mo⁵⁺ and Mo⁶⁺ respectively, which are close to those previously reported binding energies⁵⁶ with the spin-orbital splitting of 3.1 eV.⁵⁷ As the pyrolysis temperature increases, the amount of Mo⁶⁺ and Mo⁵⁺ decreases while that of Mo⁴⁺ increases. The high intensity of Mo⁴⁺ peaks in all samples evidences the presence of CoMoS_{3,13}.^{51, 58} Interestingly, the binding energy of the Mo⁴⁺ 3d_{5/2} peak for sample CoMoS-600 redshifts 0.3 eV compared to that of samples CoMoS-800 and CoMoS-1000, revealing the increase in electron density around Mo due to the electrons transferred from the less electronegative Co to Mo,⁵⁸ resulting in a stronger interaction between Co and Mo in CoMoS-600, which is beneficial to its electrochemistry performance.⁵⁹

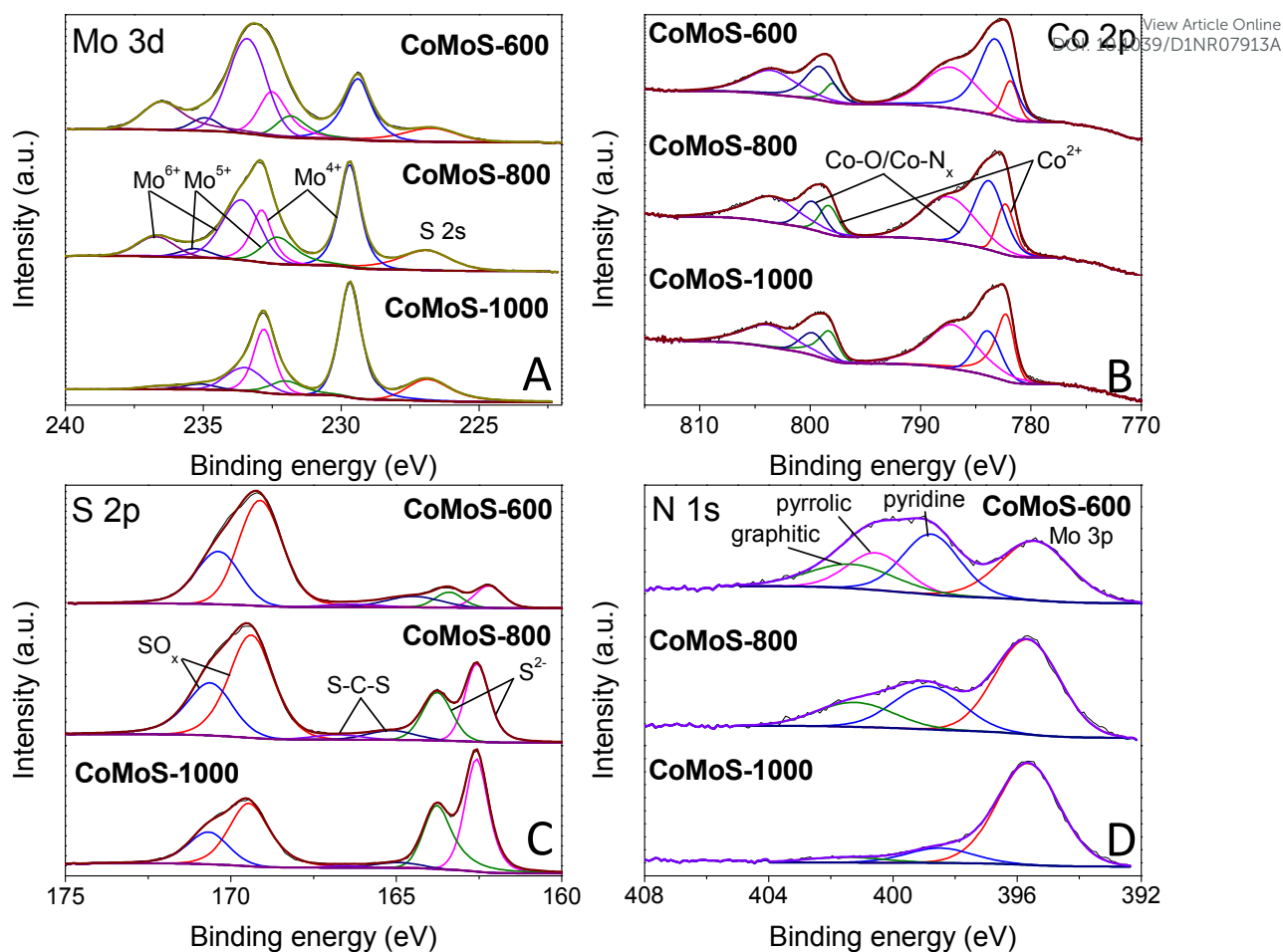


Fig. 5 High-resolution XPS spectra of A) Mo 3d, B) Co 2p, C) S 2p and D) N 1s for CoMoS-600, CoMoS-800 and CoMoS-1000.

Moreover, the XPS spectra of Co 2p for all the CoMoS samples are presented in Fig. 5B. The Co 2p peaks can be deconvoluted into three Co 2p_{3/2} and 2p_{1/2} doublets with the spin-orbit splitting of 16 eV. The peaks that appeared at around 781.9/798.0 eV ascribed to 2p_{3/2} and 2p_{1/2} of Co²⁺ respectively,²⁶ whereas the doublets at around 783.2/799.1 eV represent Co with a higher oxidation state, which is reduced as pyrolysis temperature increases. The latter can be ascribed to the formed intermediate cobalt oxide species⁶⁰ at low pyrolysis temperature, and Co-N_x species⁶¹ that originate from the combination of Co ions with N element from PDA and MeIM. It is believed that OER performance can be enhanced by the presence of Co-N_x.^{46, 62, 63} The last pair of doublets at around 787.2/803.5 eV are the shake-up satellite peaks of Co 2p.

Furthermore, high-resolution XPS spectra of S 2p are presented in Fig. 5C. Peaks at around 162.2/163.4 eV correspond to the $2p_{3/2}$ and $2p_{1/2}$ of S^{2-} ,²⁶ confirming the formation of Co-Mo-S phase. The other set of doublets at 163.4/164.5 eV is attributed to the C-S-C bond,^{64, 65} indicating the doping of the S element in the carbon matrix. It is obvious that an increased amount of S doped in the carbon matrix at low pyrolysis temperature results in enhanced modification of electronic structure and improved catalytic active sites, which are expected to improve the HER and OER performance. The doublets at 169.1/170.4 eV are attributed to oxidized S species, which is partly due to the intermediate oxide formed during the pyrolysis and partly due to the surface oxidation of the samples during the XPS inspection.^{21, 26, 66}

Lastly, the N 1s spectra of the composites are shown in Fig. 5D. Except for the Mo 3p peak at around 395.4 eV, the N 1s spectra can be deconvoluted into three peaks at around 398.8, 400.5 and 401.3 eV, which can be assigned to pyridine N, pyrrolic N and graphitic N, respectively.⁵¹ These N species indicate that the carbon matrix in the Co-Mo-S/C composites has been doped by N element, which can change the electronic structure of neighbouring carbon atoms, promoting the formation of increased catalytic active sites that can improve the HER and OER activities.^{25, 26} Similar to S-doping, the level of N-doping in the composites decreases with increasing pyrolysis temperature.

3.3 Electrochemistry performance of Co-Mo-S/C composites

The hydrogen evolution reaction (HER) performance of all the Mo-Z67-D derived samples were evaluated in 0.5 M H_2SO_4 electrolyte with a three-electrode setup. The benchmark HER catalyst 20% Pt/C as well as Z67 derived CoS-600 are also assessed for comparison. As shown by the linear sweep voltammograms (LSV) curves in Fig. 6A, the onset potential (η_{onset}) and overpotential to achieve current density of 10 mA cm^{-2} (η_{10}) for sample CoMoS-600 is -0.167 and -0.235 V respectively, apparently lower than that of samples CoMoS-800 ($\eta_{onset} = -0.206 \text{ V}$, $\eta_{10} = -0.274 \text{ V}$) and CoMoS-1000 ($\eta_{onset} = -0.251 \text{ V}$, $\eta_{10} = -0.327 \text{ V}$). Compared with CoS-

600 ($\eta_{\text{onset}} = -0.205$ V, $\eta_{10} = -0.359$ V), CoMoS-600 shows a 38 mV and 124 mV more positive onset potential and η_{10} respectively, which indicates that the introduction of PDA coating and PMA molecules have introduced a large number of active sites into the derived composites.

Moreover, the reaction kinetics of the catalysts are estimated by linear fitting of Tafel plots (Fig. 6B) derived from the polarization curves. Generally, the smaller the Tafel slope, the faster the reaction kinetics. A dramatic improvement in Tafel slope is observed for CoMoS-600 (65.50 mV dec⁻¹) compared to its Mo-free counterpart (153.24 mV dec⁻¹). Interestingly, sample CoMoS-800 shows a slightly smaller Tafel slope (61.47 mV dec⁻¹) than sample CoMoS-600, possibly due to the much higher surface area and the better conductivity of the graphitized carbon matrix of CoMoS-800. However, overall CoMoS-600 still shows the best performance among all Mo-containing composites since the electrocatalytic activities of the bimetallic Co-Mo-S/C composites are the synergistic coordination effect of the graphitization degree of the carbon matrix, the exposed active sites originated from the ultra-small nanoparticles and the amount of heteroatoms N, S and even P doping in the carbon matrix.

The electrochemical impedance spectroscopy (EIS) of the Co-Mo-S/C composites were examined to evaluate the kinetic difference of the catalysts. As shown in the Nyquist plot (Fig. 6C), all samples show depressed semi-circles, which can be modelled by an equivalent circuit consisting of series resistance (R_s), a constant phase element (CPE) and a charge-transfer resistance (R_{ct}). Sample CoMoS-600 exhibits the smallest R_{ct} of 54.75 Ω than that of CoMoS-800 (62.96 Ω) and CoMoS-1000 (86.92 Ω), which possesses a higher degree of graphitization and a better conductive substrate. This indicates that, firstly, sample CoMoS-600 possesses a better electron transferability at the interface between the electrocatalyst and the electrolyte; secondly, the number of exposed active sites from the ultra-small defect-rich nanoparticles are the dominant factor towards faster HER process for sample CoMoS-600.

In addition, the long-term stability of sample CoMoS-600 was also evaluated by the polarization curves before and after 1000 cyclic voltammetry (CV) cycles. Fig. 6D shows that the difference between the two polarization curves is negligible, which suggests good stability for sample CoMoS-600.

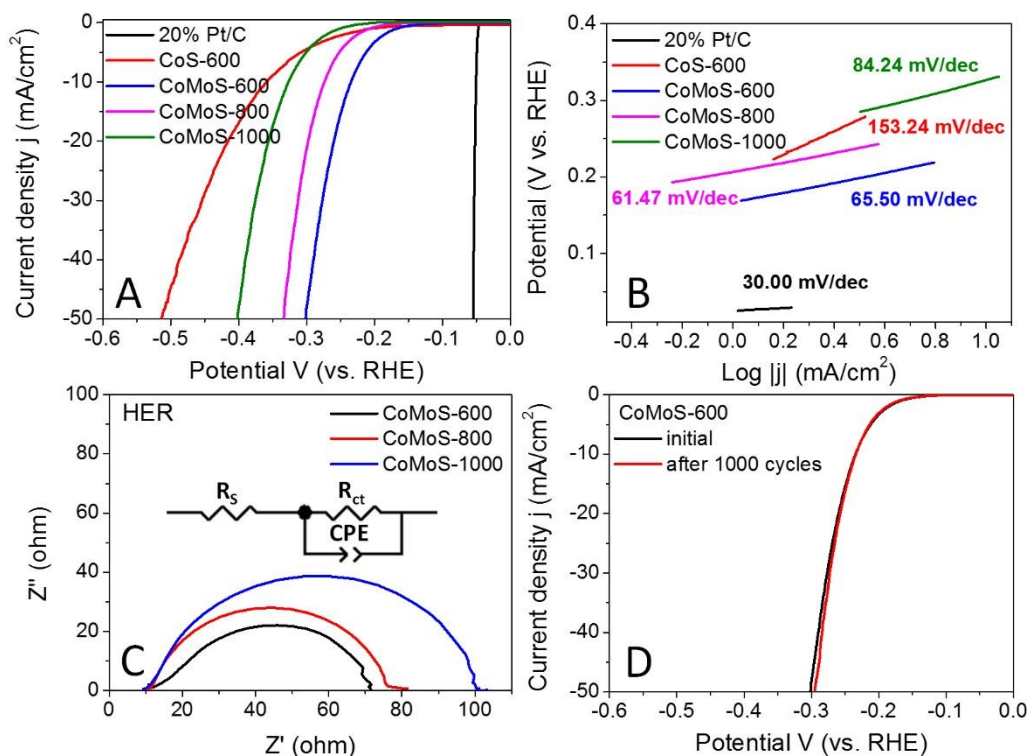


Fig. 6 A) HER polarization curves and B) corresponding Tafel plots of benchmark 20% Pt/C, CoS-600, CoMoS-600, CoMoS-800 and CoMoS-1000; C) EIS of CoMoS-600, CoMoS-800 and CoMoS-1000 and D) Polarization curves of CoMoS-600 before and after 1000 CV cycles. All polarization curves are iR corrected.

The oxygen evolution reaction (OER) catalytic activities of these bimetallic Co-Mo-S/C composites were examined in O₂ saturated 1 M KOH electrolyte at 1600 RPM, and the results are presented in Fig. 7A. All the Co-Mo-S/C composites exclusively exhibit dramatically improved OER performance compared to that of CoS-600 and the benchmark IrO₂ catalysts. Sample CoMoS-600 displays OER performance of $\eta_{\text{onset}}=0.248$ V and $\eta_{10}=0.350$ V, while sample CoMoS-800 exhibits OER performance of $\eta_{\text{onset}}=0.293$ V and $\eta_{10}=0.359$ V, which are

significantly lower than that of sample CoMoS-1000 ($\eta_{\text{onset}}=0.340$ V, $\eta_{10}=0.396$ V). Compared with Mo-free sample CoS-600 ($\eta_{\text{onset}}=0.409$ V, $\eta_{10}=0.481$ V), sample CoMoS-600 shows a prominent improvement of 161 mV downshift in onset potential and 131 mV decrease in η_{10} , which indicates that the introduced Mo-containing active sites are favourable for OER performance.

Moreover, the reaction kinetics of the catalysts towards OER are demonstrated in Fig. 7B. Sample CoMoS-800 exhibits a slightly faster reaction kinetics than sample CoMoS-600, as indicated by the smaller Tafel slope. However, overall sample CoMoS-600 is the best performed OER catalyst among the three Mo-containing composites. EIS of these Co-Mo-S/C composites were examined and fitted with a similar equivalent circuit used for the above HER (Fig. 7C). Sample CoMoS-600 exhibits the smallest R_{ct} of 45.1 Ω amongst the three Co-Mo-S/C samples, indicating that CoMoS-600 possesses the highest electron transferability in the OER process.

Furthermore, the stability of the best-performed sample, CoMoS-600, was also evaluated, and the polarization curves before and after 1000 CV cycles results are presented in Fig. 7D. A 0.01V decrease in η_{10} is observed, implying a mild improvement in OER activities after 1000 CV cycles. Moreover, XRD and SEM of the sample CoMoS-600 after 1000 CV cycles of OER measurements (see Fig. S9A and B) still show the same characteristic peaks and morphologies without obvious difference compared with the original sample, which further confirms the stability of the catalyst.

It is worth noting that the Co-Mo-S/C composites derived from Mo-Z67-D at a heating ramp rate of 2 $^{\circ}\text{C min}^{-1}$ generally exhibit slight better electrocatalytic HER and OER performance than those obtained at a heating ramp rate of 10 $^{\circ}\text{C min}^{-1}$ (Fig. S10 A and B). This may be due to the relatively higher level of graphitization of the carbon matrix obtained at a

slower heating ramp rate (Table S2), which provides a relatively better charge transferability during the electrocatalytic process compared to the sample obtained at a fast heating ramp rate.

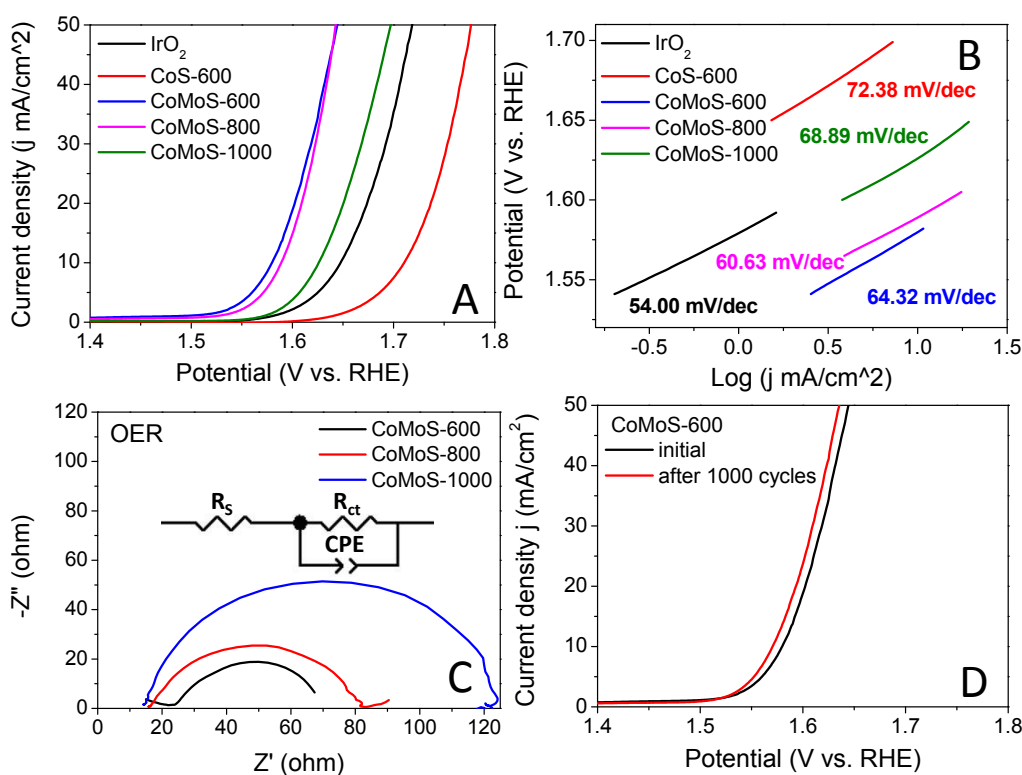


Fig. 7 A) OER polarization curves and B) corresponding Tafel plots of the benchmark IrO₂, CoS-600, CoMoS-600, CoMoS-800 and CoMoS-1000. C) EIS of CoMoS-600, CoMoS-800 and CoMoS-1000. D) Polarization curves of CoMoS-600 before and after 1000 CV cycles. All polarization curves are iR corrected.

Based on the electrocatalytic performance and the material characterization results, the remarkable improvement in electrocatalytic performance of the bimetallic Co-Mo-S/C composite obtained at 600°C can be ascribed to the synergistic effect of following factors: 1) the evenly distributed ultra-small defect-rich Co-Mo-S phase nanoparticles that maximize the active-surface-area-to-volume-ratio and increase the number of exposed active sites; the abundant lattice distortions, defects in the ultra-small nanoparticles are active sites for HER and OER^{16, 17}; 2) heteroatoms including S element from H₂S gas, as well as N element from

PDA coating and organic linker in ZIF-67, even trace amount of P derived from PMA, lead to heteroatom N and S-doped composites, which modulates the electronic structure of neighbouring C atoms and provides enhanced active sites for HER and OER^{25, 26}; 3) the strong interaction between Co and Mo in the Co-Mo-S phase improve the electron conductivity of the composites and is favourable for the charge transfer during the electrocatalytic reaction^{58, 59}; and 4) the porous carbon support offers high surface area and provides access routes to the reaction active sites, facilitate the easy mass transportation during the electrocatalytic reaction^{22, 23}.

3.4 Characterization and electrocatalytic performance of bimetallic Co-W-S/C composites derived from PTA@ZIF-67@PDA nanocubes

The same synthesis approach is further expanded to synthesize phosphotungstic acid (PTA)@ZIF-67@PDA to demonstrate the generalization of this material synthesis method. As shown in Fig. 1D, the TEM image of the as-obtained PTA@ZIF-67@PDA, i.e. W-Z67-D, shows a slightly different morphology from the parental Z67-D sample that lamellar petal-like W-PDA complex with greater thickness is coated on the cubes with random free-end protruding, no hollow cavity is observed in the core. Obviously, no observable dissociation of ZIF-67 occurred. The presence of homogeneous and intact core in W-Z67-D indicates that the addition of the same weight amount of PTA does not etch the core of the composite nor alter the structure and morphology of ZIF-67. The elemental mappings of W-Z67-D (Fig S1D) show that O, P and W elements mostly accumulate on the surface of the nanocubes, whereas N and Co elements distribute evenly across the cubes, indicating that majority of PTA molecules are chelated with the coated PDA. The corresponding elemental line scanning (Fig. S2D) also supports this conclusion. Both XRD patterns (Fig. S3A) and FT-IR spectra (Fig. S3B) support that the PTA has been successfully introduced into the PDA decorated ZIF-67 composites without changing the structure of ZIF-67. W-Z67-D possesses a S_{BET} close to that of Z67-D,

suggesting that PTA etching does not occur and extra hierarchical pores are not generated by the introduction of PTA.

The as-obtained W-Z67-D was also subjected to pyrolysis at different temperatures in H₂S/Ar atmosphere with different heating ramp rates. The XRD patterns (Fig. S11) suggest that the derivatives are composed of defect-rich Co_{1-x}S and WS₂ nanocrystals, and no metal oxide is observed. The Raman spectra (Fig. S5C and D) of the W-Z67-D derivatives and their I_D/I_G ratios (Table S2) are similar to the Mo-Z67-D derivatives, and slower heating ramp rate results in a higher degree of graphitization of the carbon matrix. Compared with Mo-Z67-D derived composites, W-Z67-D derived Co-W-S/C composites show a similar agglomeration and crystallization trend as the pyrolysis temperature increases. The TEM images and elemental mappings of the Co-W-S/C composites are presented in Fig. S12 and Fig. S13 respectively. TEM images suggest the presence of Co_{1-x}S crystals and WS₂ flakes in the Co-W-S/C composites, and elemental mappings confirm the homogeneous distribution of all elements.

Unsurprisingly, Co-W-S/C composites also show enhanced electrocatalytic activities towards HER and OER but with completely different performance orders for the samples (Fig. S14 and Table S5). Composite CoWS-800 exhibits the best HER activity, while composite CoWS-1000 displays the highest OER performance amongst the samples obtained at different pyrolysis temperatures, which is consistent with the performance of one-pot synthesized POM@ZIF-67 derived WS₂/Co_{1-x}S/N, S co-doped porous carbon reported by our group previously.²⁶ It is believed that the different order of performance between PMA and PTA@ZIF-67@PDA derivatives are due to i) the different types of active sites in the composites and ii) the different morphologies of the composites derived under the same temperature. However, the effect of the heating ramp rate on the electrocatalytic performance of the Mo-Z67-D derived samples and W-Z67-D derivatives are the same. That sample

obtained at a slow heating ramp rate shows a slightly better electrocatalytic performance (Fig. S10 C and D). It is again likely due to the relatively higher degree of graphitization of the carbon matrix obtained at a slower heating ramp rate (Table S2) that provides a relative better charge transferability during the electrochemical reaction process.

4. Conclusions

In summary, we have successfully developed a generalized approach to synthesize both HER and OER active, defect-rich ultra-fine bimetallic Co-Mo sulfide nanoparticles supported on N, S-doped porous carbon composites from PMA@ZIF-67@PDA nanocubes via carbonization/sulfurization. PDA decorating on ZIF-67 cubes can prevent the over-dissociation of ZIF-67 from PMA etching by chelating with the PMA molecules, and acts as an additional N source for N-doping. Moreover, the partially dissociated Co^{2+} from ZIF-67 can be captured by the coated PDA via chelation, resulting in more evenly dispersed active sites throughout the heterogeneous composite after pyrolysis. The resulting bimetallic CoMoS-600 composite exhibits remarkable improvement in HER (with overpotential of -0.235 V vs. RHE at current density of 10 mA cm^{-2} and Tafel slope of $65.50 \text{ mV dec}^{-1}$) and OER performance (with overpotential of 0.350 V vs. RHE at current density of 10 mA cm^{-2} and Tafel slope of $64.32 \text{ mV dec}^{-1}$). The outstanding performance can be attributed to the synergistic effect of ultra-fine and defect-rich Co-Mo-S nanoparticle exposed active sites and N, S-doped porous carbons in the composites. Moreover, HER and OER active W-containing bimetallic Co-W-S/C composites can be readily obtained by replacing PMA with PTA, proving the universality of this synthesis approach. This work offers a new synthesis strategy to modify acid-sensitive ZIFs with acidic compounds, providing an alternative approach to develop other advanced metal sulfides/porous carbon functional materials for energy and environmental applications.

Conflicts of interest

View Article Online
DOI: 10.1039/D1NR07913A

The authors declare no conflict of interest.

Author contributions

Zheng Huang: Investigation, Methodology, Data curation; Writing - original draft. Zhuxian Yang: Investigation, Data curation, Validation, Writing - review & editing. Quanli Jia: Investigation, Validation, Data curation. Nannan Wang: Investigation, Validation, Data curation. Yanqiu Zhu: Supervision, Writing - review & editing. Yongde Xia: Supervision, Conceptualization, Methodology, Validation, Writing - review & editing.

Acknowledgements

This work was supported by the EPSRC Doctoral Training Partnership at University of Exeter, Leverhulme Trust (RPG-2018-320) and Royal Society (IEC\NSFC\201121).

References

1. G. Kakoulaki, I. Kougias, N. Taylor, F. Dolci, J. Moya and A. Jäger-Waldau, *Energy Convers. Manag.*, 2021, **228**, 113649.
2. M. Z. Hussain, B. van der Linden, Z. Yang, Q. Jia, H. Chang, R. A. Fischer, F. Kapteijn, Y. Zhu and Y. Xia, *J. Mater. Chem. A*, 2021, **9**, 4103-4116.
3. M. Z. Hussain, Z. Yang, Z. Huang, Q. Jia, Y. Zhu and Y. Xia, *Adv. Sci.*, 2021, **8**, 2100625.
4. M. Z. Hussain, Z. Yang, B. v. d. Linden, Z. Huang, Q. Jia, E. Cerrato, R. A. Fischer, F. Kapteijn, Y. Zhu and Y. Xia, *J. Energy Chem.*, 2021, **57**, 485-495.
5. N. K. Oh, J. Seo, S. Lee, H.-J. Kim, U. Kim, J. Lee, Y.-K. Han and H. Park, *Nat. Commun.*, 2021, **12**, 4606.
6. X. Chia, A. Y. S. Eng, A. Ambrosi, S. M. Tan and M. Pumera, *Chem. Rev.*, 2015, **115**, 11941-11966.

7. X. Wu, H. Zhang, J. Zhang and X. W. Lou, *Adv. Mater.*, 2021, **33**, 2008376. View Article Online
DOI: 10.1039/D1NR07913A
8. P. Zhuang, Y. Sun, P. Dong, W. Smith, Z. Sun, Y. Ge, Y. Pei, Z. Cao, P. M. Ajayan, J. Shen and M. Ye, *Adv. Funct. Mater.*, 2019, **29**, 1901290.
9. X. Zhang, F. Zhou, S. Zhang, Y. Liang and R. Wang, *Adv. Sci.*, 2019, **6**, 1900090.
10. E. German and R. Gebauer, *Appl. Surf. Sci.*, 2020, **528**, 146591.
11. Y. Li, Z. Yin, M. Cui, X. Liu, J. Xiong, S. Chen and T. Ma, *J. Mater. Chem. A*, 2021, **9**, 2070-2092.
12. H. Wang, W. Zhang, X. Zhang, S. Hu, Z. Zhang, W. Zhou and H. Liu, *Nano Res.*, 2021, **14**, 4857-4864.
13. W.-H. Huang, X.-M. Li, X.-F. Yang, H.-B. Zhang, F. Wang and J. Zhang, *Chem. Commun.*, 2021, **57**, 4847-4850.
14. V. Ganesan and J. Kim, *Int. J. Hydrogen Energy*, 2020, **45**, 13290-13299.
15. Y. Guo, J. Tang, Z. Wang, Y.-M. Kang, Y. Bando and Y. Yamauchi, *Nano Energy*, 2018, **47**, 494-502.
16. C.-A. Chen, C.-L. Lee, P.-K. Yang, D.-S. Tsai and C.-P. Lee, *Catalysts*, 2021, **11**, 151.
17. R. Abinaya, J. Archana, S. Harish, M. Navaneethan, S. Ponnusamy, C. Muthamizhchelvan, M. Shimomura and Y. Hayakawa, *RSC Adv.*, 2018, **8**, 26664-26675.
18. H. Wang, Z. Xu, Z. Zhang, S. Hu, M. Ma, Z. Zhang, W. Zhou and H. Liu, *Nanoscale*, 2020, **12**, 22541-22550.
19. L. Wang, L. Wang, X. Meng and F.-S. Xiao, *Adv. Mater.*, 2019, **31**, 1901905.
20. Y. Jazaa, T. Lan, S. Padalkar and S. Sundararajan, *Lubricants*, 2018, **6**, 106.
21. Z. Huang, Z. Yang, M. Z. Hussain, Q. Jia, Y. Zhu and Y. Xia, *J. Mater. Sci. Technol.*, 2021, **84**, 76-85.
22. X. Zheng, J. Xu, K. Yan, H. Wang, Z. Wang and S. Yang, *Chem. Mater.*, 2014, **26**, 2344-2353.

23. H. Li, K. Yu, C. Li, Z. Tang, B. Guo, X. Lei, H. Fu and Z. Zhu, *Sci. Rep.*, 2015, **5**, 18730. Article Online
DOI: 10.1039/D1NR07913A
24. T. Rodenas, S. Beeg, I. Spanos, S. Neugebauer, F. Girgsdies, G. Algara-Siller, P. P. M. Schleker, P. Jakes, N. Pfänder, M. Willinger, M. Greiner, G. Prieto, R. Schlögl and S. Heumann, *Adv. Energy Mater.*, 2018, **8**, 1802404.
25. X. Yu, M. Zhang, J. Chen, Y. Li and G. Shi, *Adv. Energy Mater.*, 2016, **6**, 1501492.
26. Z. Huang, Z. Yang, M. Z. Hussain, B. Chen, Q. Jia, Y. Zhu and Y. Xia, *Electrochim. Acta*, 2020, **330**, 135335.
27. S. Gao, J. Hou, Z. Deng, T. Wang, S. Beyer, A. G. Buzanich, J. J. Richardson, A. Rawal, R. Seidel, M. Y. Zulkifli, W. Li, T. D. Bennett, A. K. Cheetham, K. Liang and V. Chen, *Chem*, 2019, **5**, 1597-1608.
28. J. Javidi, M. Esmaeilpour, Z. Rahiminezhad and F. N. Dodeji, *J. Cluster Sci.*, 2014, **25**, 1511-1524.
29. H. Wei, J. Ren, B. Han, L. Xu, L. Han and L. Jia, *Colloids Surf. B*, 2013, **110**, 22-28.
30. P. Zhou, J. Cheng, Y. Yan, S. Xu and C. Zhou, *Sep. Purif. Technol.*, 2021, **272**, 118871.
31. H. B. Wu, B. Y. Guan, P. He and X.-Y. Yu, *J. Mater. Chem. A*, 2018, **6**, 19338-19341.
32. Z. Zhu, R. Tain and C. Rhodes, *Can. J. Chem.*, 2003, **81**, 1044-1050.
33. A. Patel, N. Narkhede and A. Patel, *Catal. Surv. Asia*, 2019, **23**, 257-264.
34. K. M. Im, T.-W. Kim and J.-R. Jeon, *ACS Biomater. Sci. Eng.*, 2017, **3**, 628-636.
35. L. Sun, C. Wang, X. Wang and L. Wang, *Small*, 2018, **14**, 1800090.
36. J. Qin, S. Wang and X. Wang, *Appl. Catal. B*, 2017, **209**, 476-482.
37. W. Kong, J. Li, Y. Chen, Y. Ren, Y. Guo, S. Niu and Y. Yang, *Appl. Surf. Sci.*, 2018, **437**, 161-168.
38. M. Zhang, C. Wang, R. Luo, W. Zhang, S. Chen, X. Yan, J. Qi, X. Sun, L. Wang and J. Li, *J. Mater. Chem. A*, 2019, **7**, 5173-5178.
39. B. Chen, R. Li, G. Ma, X. Gou, Y. Zhu and Y. Xia, *Nanoscale*, 2015, **7**, 20674-20684.

40. P. Muhammed Shafi and A. Chandra Bose, *AIP Adv.*, 2015, **5**, 057137. View Article Online
DOI: 10.1039/D1NR07913A
41. K. N. Kudin, B. Ozbas, H. C. Schniepp, R. K. Prud'homme, I. A. Aksay and R. Car, *Nano Lett.*, 2008, **8**, 36-41.
42. A. C. Ferrari and J. Robertson, *Phys. Rev. B*, 2000, **61**, 14095-14107.
43. D. B. Schuepfer, F. Badaczewski, J. M. Guerra-Castro, D. M. Hofmann, C. Heiliger, B. Smarsly and P. J. Klar, *Carbon*, 2020, **161**, 359-372.
44. L. Deng, Z. Yang, R. Li, B. Chen, Q. Jia, Y. Zhu and Y. Xia, *Front. Chem. Sci. Eng.*, 2021, **15**, 1487-1499.
45. D. H. Kweon, M. S. Okyay, S.-J. Kim, J.-P. Jeon, H.-J. Noh, N. Park, J. Mahmood and J.-B. Baek, *Nat. Commun.*, 2020, **11**, 1278.
46. H. Han, Z. Bai, T. Zhang, X. Wang, X. Yang, X. Ma, Y. Zhang, L. Yang and J. Lu, *Nano Energy*, 2019, **56**, 724-732.
47. F. Yang, P. Zhao, X. Hua, W. Luo, G. Cheng, W. Xing and S. Chen, *J. Mater. Chem. A*, 2016, **4**, 16057-16063.
48. Y. Zhong, Y. Zhang, G. Zhang, R. Li and X. Sun, *Appl. Surf. Sci.*, 2012, **263**, 410-415.
49. P. Mallet, H. Guyot, J. Y. Veullen and N. Motta, *Phys. Rev. B*, 2001, **63**, 165428.
50. Z. Chen, A. Liao, Z. Guo, F. Yu, T. Mei, Z. Zhang, M. S. Irshad, C. Liu, L. Yu and X. Wang, *Electrochim. Acta*, 2020, **353**, 136561.
51. S. H. Yang, S.-K. Park, J. K. Kim and Y. C. Kang, *J. Mater. Chem. A*, 2019, **7**, 13751-13761.
52. R. Wei, K. Zhang, P. Zhao, Y. An, C. Tang, C. Chen, X. Li, X. Ma, Y. Ma and X. Hao, *Appl. Surf. Sci.*, 2021, **549**, 149327.
53. J. Xie, X. Yang and Y. Xie, *Nanoscale*, 2020, **12**, 4283-4294.
54. W. Hong, M. Kitta and Q. Xu, *Small Methods*, 2018, **2**, 1800214.

55. F. Bu, W. Chen, M. F. Aly Aboud, I. Shakir, J. Gu and Y. Xu, *J. Mater. Chem. A*, 2019, **7**, 14526-14535. View Article Online
DOI: 10.1039/D1NR07913A
56. Y. Sun, J. Wang, B. Zhao, R. Cai, R. Ran and Z. Shao, *J. Mater. Chem. A*, 2013, **1**, 4736-4746.
57. J.-W. Shi, Y. Zou, D. Ma, Z. Fan, L. Cheng, D. Sun, Z. Wang, C. Niu and L. Wang, *Nanoscale*, 2018, **10**, 9292-9303.
58. C. Ray, S. C. Lee, K. V. Sankar, B. Jin, J. Lee, J. H. Park and S. C. Jun, *ACS Appl. Mater. Interfaces*, 2017, **9**, 37739-37749.
59. X. Ma, W. Chen, Q. Li, L. Xue and C. Peng, *Energy Environ. Mater.*, 2021, **4**, 658-663.
60. J. Zhang, D. Meng, H. Huang, H. Cai, Q. Huang, J. Wang, Y. Yang, X. Zhai, Z. Fu and Y. Lu, *AIP Adv.*, 2018, **8**, 025322.
61. X. Cui, W. Li, K. Junge, Z. Fei, M. Beller and P. J. Dyson, *Angew. Chem. Int. Ed.*, 2020, **59**, 7501-7507.
62. A. Macedo Andrade, Z. Liu, S. Grewal, A. J. Nelson, Z. Nasef, G. Diaz and M. H. Lee, *Dalton Trans.*, 2021, **50**, 5473-5482.
63. B. Chen, X. He, F. Yin, H. Wang, D.-J. Liu, R. Shi, J. Chen and H. Yin, *Adv. Funct. Mater.*, 2017, **27**, 1700795.
64. J. Cui, Y. Qiu, H. Zhang, Z. Yao, W. Zhao, Y. Liu and J. Sun, *Solid State Ion.*, 2021, **361**, 115548.
65. A. Abdul Razzaq, Y. Yao, R. Shah, P. Qi, L. Miao, M. Chen, X. Zhao, Y. Peng and Z. Deng, *Energy Storage Mater.*, 2019, **16**, 194-202.
66. G. Li, J. Sun, W. Hou, S. Jiang, Y. Huang and J. Geng, *Nat. Commun.*, 2016, **7**, 10601.